Indentation fracture of low-dielectric constant films: Part I. Experiments and observations

Dylan J. Morris[a] and Robert F. Cook

Materials Science and Engineering Laboratory, National Institute of Standards and Technology, Gaithersburg, Maryland 20899-8520

Advanced microelectronic interconnection structures will need dielectrics of low permittivity to reduce capacitive delays and crosstalk, but this reduction in permittivity typically necessitates an increase in the porosity of the material, which is frequently accompanied by reduced mechanical reliability. Failure by brittle fracture remains a typical manufacturing and reliability hurdle for this class of materials. Part I of this two-part work explores the instrumented indentation and indentation fracture responses of a variety of organosilicate low-dielectric constant (low-κ) films. Three different chemical varieties of low-κ material were tested. The influence of film thickness on the fracture response is also explored systematically. Correlations are made between instrumented indentation responses and differing modes of fracture. It is demonstrated that the elastic response of the composite film + substrate systems can be simply tied to the fraction of the total indentation strain energy in the film. These results are then used in the companion paper, Part II [D.J. Morris and R.F. Cook, *J. Mater. Res.* **23**, 2443 (2008)], to derive and use a fracture mechanics model to measure fracture properties of low-κ films.

I. INTRODUCTION

Incorporation of low-dielectric constant (low-κ) materials into silicon-based integrated circuits is a major technological challenge facing the microelectronics industry. As the required permittivity of the dielectric material in the back-end-of-line interconnection structure approaches that of a vacuum, it is inevitable that the density of the dielectric material falls, no matter what its chemical makeup. However, the dielectric material functions as a structural material in integrated circuits, and the reduction of density has important consequences for the mechanical properties of these materials. Improvement of the fracture toughness T of low-κ dielectrics remains a difficult challenge, according to the current International Technology Roadmap for Semiconductors.[1] Certainly, then, a method to quantitatively measure the fracture toughness of low-κ dielectrics is needed. In this work, the extension of a well-established method for fracture toughness estimation, indentation fracture,[2,3] is described.

Part I of this two-part work summarizes indentation experiments that were performed on various organosili-cate low-κ material films with the goal of measuring film fracture toughness. There are several hurdles to studying the fracture properties of low-κ films. Principally, it must be verified that sharp indentation can be used to create controlled flaws in low-κ materials. The low-dielectric constant—and accompanying inclusion of porosity (or increased openness of the molecular structure)—will almost certainly mean that the conventional residual-stress elastic-plastic mechanism of radial indentation fracture will not work for these materials.[4] The conventional indentation fracture model depends on volume-conserving plastic deformation, a condition that is only met with fully dense ceramics and glasses.

In addition, practical considerations within the microelectronics industry dictate that organosilicate low-κ materials normally exist only in thin film form and that the substrate be silicon, even for the purposes of mechanical testing. Two obvious consequences of this necessary material arrangement on indentation fracture are (i) there will, in general, be pre-existing stresses in the film, typically tensile in low-κ films, and (ii) the shape development of the indentation flaws will be constrained, as the cracks are arrested or shaped by the (presumably) much tougher substrate underneath.

The results of this work outline experimental results and procedures for performing and measuring the fracture response of thin, low-κ films, which are significantly more involved than the usual indentation fracture method

of measuring crack length versus indentation load. The fracture responses are shown to have no clear scaling trends, in contrast to most indentation fracture models. Information from instrumented indentation, such as load–displacement traces and the derived elastic moduli, are crucial in determining which data are even potentially analyzable in a radial-cracking fracture model. Furthermore, the variation of apparent elastic modulus with increasing indentation load is shown to follow analytical energy-partitioning theories, which will be useful in the fracture mechanics model developed in the companion paper, Part II.[5]

II. MATERIALS AND EXPERIMENTAL PROCEDURES

A. Materials

Three varieties of low-κ films were supplied by International SEMATECH (Austin, TX) on 700-μm-thick $\langle 100 \rangle$-oriented silicon substrates. They are designated by generic names of LK ("low-κ") A, B, and C. Material LKA was a chemical-vapor deposited (CVD) organosilicate material, $\kappa \simeq 2.8$. Material LKB ($\kappa \simeq 2.2$) was a methyl-silsesquioxane (MSQ) based material, formed by spin-on processing techniques. Materials LKC-1 ($\kappa \simeq 2.4$) and LKC-2 ($\kappa \simeq 2.0$) were a third variety of spin-on low-κ material, chemically identical, except for the amount of incorporated porosity (as a means of controlling the dielectric constant). All three materials were commercially available and under evaluation by SEMATECH as candidates for use in microelectronic devices. Table I lists each low-κ material, SEMATECH-reported film thicknesses t^F and film stress σ^F (measured by wafer-curvature methods), and indentation modulus $\bar{E}^F$ and hardness H^F as determined from Berkovich indentation. The film stress is only known for three thicknesses of LKA. The reported hardness of the film is the minimum observed hardness over a range of indentation depths, and the reported indentation modulus (typically identified as the plane-strain elastic modulus for an isotropic material), $\bar{E}^F = E^F/[1 - (\nu^F)^2]$ is determined as described in Sec. IV.

B. Experimental methods

Indentation experiments were performed using as many as four different-shaped sharp diamond probes, varying in acuity from the Berkovich to the cube-corner.

The geometry of these probes is summarized in Morris et al.[6] From here, we refer to the indenters by their common name (Berkovich, cube-corner) or the effective axisymmetric equivalent axis-to-edge angle. The axisymmetric equivalent is the right cone that has the same proportionality of the projected area to the square of the distance from the apex as the ideal three-sided pyramid. For instance, the ideal cube-corner has an axisymmetric equivalent angle of 42.3°, and the Berkovich has an axisymmetric equivalent angle of 70.3°. The intermediate 3-sided pyramids have axisymmetric equivalents of 49.6° and 58.9°.

All indentations were performed with the following schedule: loading at constant indentation strain rate of 0.050 s^{-1},[7] 5 s hold at maximum load, unloading to 10% of maximum load in 30 s, and a 30 s hold to calculate the thermal drift rate[8] before complete unloading. Continuous stiffness measurements[9] were made during the loading and peak-load hold with a superimposed 2-nm amplitude sinusoidal oscillation at 45 Hz.

Indentation fracture experiments were performed with the 49.6°, 58.9°, and cube-corner probes, using the NanoIndenter XP (MTS Corp, Oak Ridge, TN). Maximum indentation loads were chosen to be evenly spaced on a logarithmic plot, for instance, peak loads of 0.1, 0.15, 0.22, 0.32, 0.46, and 0.68 mN between 0.1 and 1.0 mN. Five indentations were made to each peak load.

Berkovich indentation experiments were performed on many of the films with the NanoIndenter DCM module. The purpose of these experiments was to glean elastic and plastic information about the film using standard modulus and hardness determination techniques.[10] The Berkovich indenter tip-shape and column compliance (for the DCM module) was calibrated with fused silica with the proprietary MTS software. The tip shape for the more acute 49.6°, 58.9°, and cube-corner probes was assumed to be perfect when calculating indentation modulus or hardness, due to known problems with Oliver–Pharr inferential tip-shape calibration when there is fracture at the indentation.[6,11]

Field-emission-source scanning electron microscopy (SEM) was used to image each indentation of interest. A conductive 5-nm Pt coating was sputtered on each film after indentation but before imaging. It was discovered early that low-κ materials were susceptible to damage and etching when subjected to high magnification (most

TABLE I. Properties of low-dielectric constant materials.

Material	κ	t^F (μm)	σ^F (MPa)	H^F (GPa)	$\bar{E}^F$ (GPa)
LKA	2.8	2.0, 1.5, 1.0, 0.5	58.2, 61.2, 63.6, . . .	1.5	9.3
LKB	2.2	2.4, 1.6, 1.2	. . .	0.4	3.1
LKC-1	2.4	1.0	. . .	0.5	3.8
LKC-2	2.0	1.0	. . .	0.2	1.8

often greater than 10,000×) imaging. Sample damage was kept to an acceptable threshold by keeping beam acceleration voltages small (<2.0 kV) and imaging times short (<1 min). A small amount of electron-beam etching of the film is unavoidable but beneficial; indentation crack contrast was greatly increased. The apparent length of the cracks was never observed to increase with increasing beam damage until beam damage was so extensive as to significantly distort the entire image.

III. RESULTS

A. Indentation fracture

1. Initial fracture observations

Some initial exploratory experiments were performed on 1.0-μm LKC-1 with the Berkovich and cube-corner probes. It is preferable to study fracture with the Berkovich probe, if possible, due to the widespread availability and usage, as well as the large body of literature exploring indentation mechanics, of the Berkovich (and the four-sided analogue, the Vickers) in particular. The cube-corner is perhaps the next most popular sharp probe geometry for depth-sensing indentation and has mostly been utilized for its fracture-generating power in small volumes and thin films. While it is well known that the greater acuity of the cube-corner decreases the indentation fracture threshold load (the load beneath which the material will not crack) P_{th} for bulk materials by a great deal,[12–14] it is also known that the threshold indentation load for radial fracture can decrease markedly with toughness, normally recognized as a $P_{th} \sim T^4$ relationship.[15–18] Because the toughness of silicate low-κ materials is expected to decrease commensurately with porosity, these competing effects suggest that Berkovich indentation could potentially be used to study fracture for these materials.

Figure 1 compares Berkovich and cube-corner indentations on LKC-1 with film thickness $t^F = 1.0$ μm. Figures 1(a) and 1(b) are SEM images of 5- and 50-mN Berkovich indentations. To the right of each image is a schematic diagram of an impression left by a three-sided pyramid, the projected area of which was calculated using the Oliver–Pharr method[10] from the contact depth and tip-shape function. The micrographs all show crack-like features. However, comparison with the calculated area of the indentation impression shows that what might be radial fracture at a first glance is, in fact, cutting and crushing where the probe has contacted the material. Figure 1(c) compares the micrograph of the cube-corner indentation to the projected contact area. The crack length c is defined in the conventional way; from the center of the impression to the crack tip, as shown in the figure. From these results, it was concluded that the Berkovich is, most likely, insufficiently acute to generate

real radial fracture even in low-κ films of usual (micrometer-level) thickness. Therefore, further indentation fracture was focused on the indentation fracture phenomena of more acute probes; in particular, the cube-corner geometry.

2. Crack length as a function of indentation load

Figure 2(a) is a plot of crack length versus indentation load (c-P) on logarithmic scales of cube-corner fracture on 2.0-, 1.5-, 1.0-, and 0.5-μm-thick LKA. In this and following figures, a data point represents the mean, and error bars one standard deviation in measured crack length; where not seen, the error bars are smaller than the symbol size. The conventional residual elastic-plastic field model of indentation fracture[3,19] shows that c will vary as $P^{2/3}$ for a homogeneous, ideally brittle, material. The $P^{2/3}$ slope is shown on Fig. 2(a) for comparison to the data.

Some quick observations may be made about the fracture data of Fig. 2(a). First, $c \sim P^{2/3}$ scaling is not observed over any significant range of indentation load for any film, nor is any simple scaling evident. For example, the 2.0-μm-thick LKA cube-corner fracture response scales approximately as $c \sim P$ at the smallest indentation loads, and roughly $c \sim P^{2/5}$ in the region between 1.0 and 4.6 mN. Also, there is a clear effect of the film thickness on the fracture response; cracks are usually longer at fixed indentation load in the thicker film. However, this is not always so; it can be seen in Fig. 2(a) that at the smallest loads, crack lengths at the smallest indentation loads were slightly larger in the 1.5-μm film than they were in the 2.0-μm-film. It is also noted that for all films that there was a "jump" in the crack length (a seemingly discontinuous rise in the measured radial crack length) above a certain indentation load—for example; between 4.6 and 6.8 mN for 2.0-μm-thick LKA, and between 0.68 and 1.0 mN for 0.5-μm-thick LKA.

The radial crack-length jump above some certain load was a common (not universal) feature of indentation fracture on low-κ films. The discontinuous nature of the c-P response at that point suggests that some energetic barrier had been overcome, or the cracks had taken on a new configuration. Therefore considerable effort was expended in finding the nature of the crack-length jump in an effort to determine what data can be analyzed in a fracture mechanics framework.

Figure 2(b) is a c-P plot on logarithmic scales of cube-corner fracture on 2.4-, 1.6-, and 1.2-μm-thick LKB. As was seen in Fig. 2(a) for LKA, the c-P response does not follow any simple scaling laws, but there is a similar decrease in the sensitivity of the crack length to increasing indentation load. The effect of film thickness on the LKB fracture response is less clear than for LKA; while the 2.4-μm film has a smaller threshold load for fracture
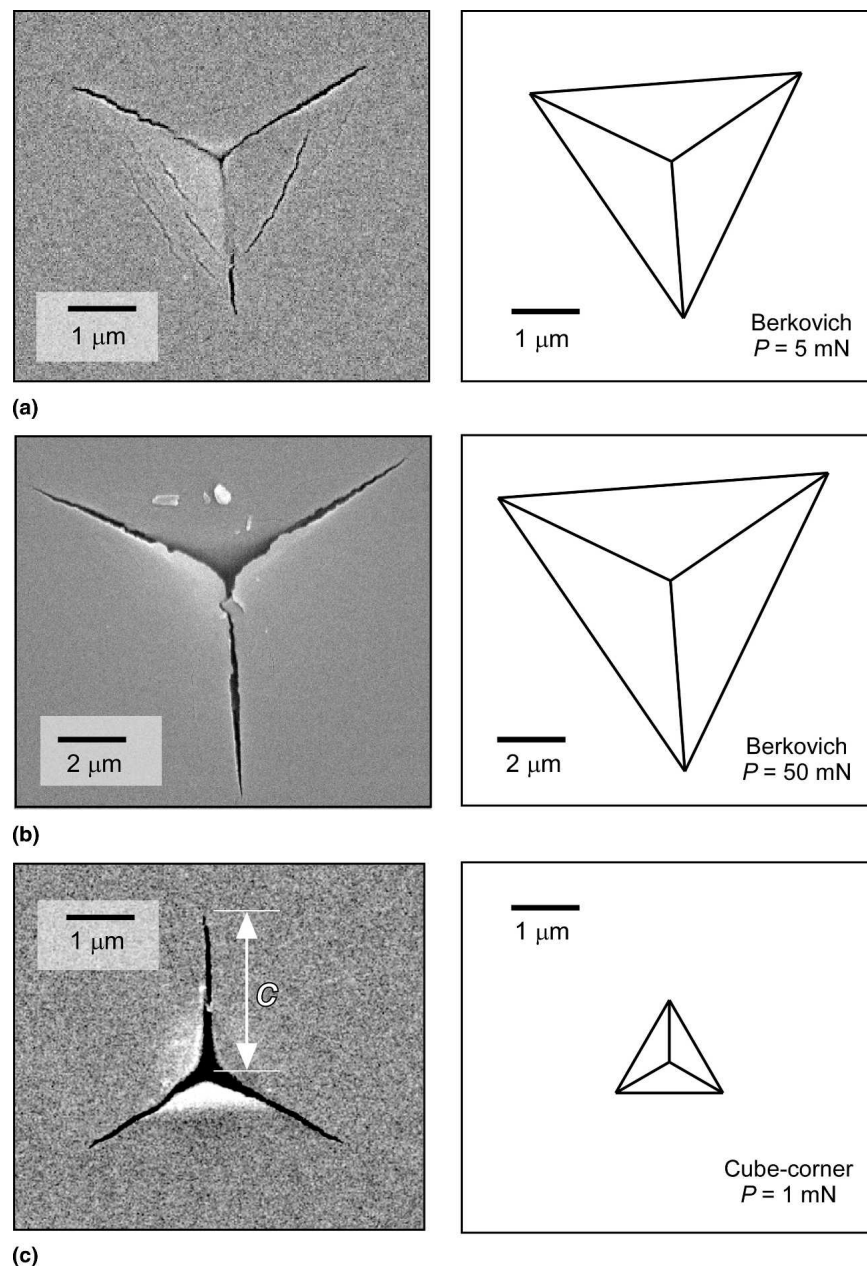
FIG. 1. (Left) SEM image, (right) contact area calculated by Oliver–Pharr method. (a) 5-mN peak load Berkovich indentation on 1-μm LKC-1. (b) 50-mN peak load Berkovich indentation on 1-μm-thick LKC-1. (c) 1-mN peak load cube-corner indentation on 1-μm LKC-1. The crack length is defined as the distance from the impression center to the crack tip.

and typically longer cracks over the entire load range, cracks in the 1.2-μm film are longer than either of the two thicker films at $P = 0.15$ mN.

Figure 2(c) compares the cube-corner fracture response of 1-μm-thick LKC-1 and LKC-2. One would imagine that the toughness of LKC-2 is lower than LKC-1—the only nominal difference between the materials is that LKC-2 is less dense—but there is no clear distinction between the films from the fracture response over the entire load range. In fact, LKC-1 has a smaller threshold load than LKC-2.

Figure 2(d) is a c-P plot for 2.4-μm-thick LKB for fracture generated with the cube-corner [the same data as in Fig. 2(b)], as well as with the less acute 49.6° and 58.9° probe geometries. As the indenting probe becomes more obtuse, the threshold load for fracture increases dramatically: a factor of about four increase from the cube-corner to the 49.6° probe, and a further factor of five increase from the 49.6° to the 58.6° probe. After radial cracking initiated, the c-P responses converged with increasing load. At larger loads, there was a well-defined jump in crack length, exactly as seen for
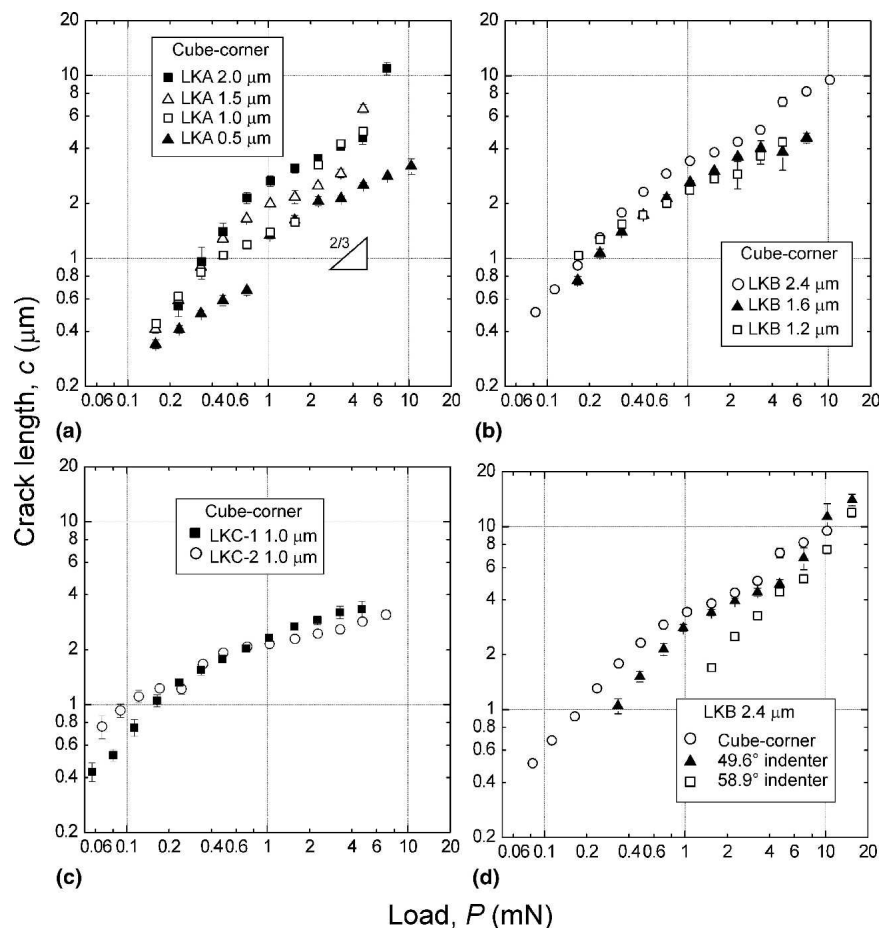
FIG. 2. (a) c-P response of cube-corner indentation on 2.0-, 1.5-, 1.0-, and 0.5-μm-thick LKA. (b) c-P response of cube-corner indentation on 2.4-, 1.6-, and 1.2-μm-thick LKB. (c) c-P response of cube-corner indentation on 1.0-μm-thick LKC-1 and LKC-2. (d) c-P response of cube-corner, 49.6° and 58.9° on 2.4-μm-thick LKB.

cube-corner indentation on LKA [Fig. 2(a)]. While the indentation load for the crack-length jump decreased slightly with increased probe acuity, the radial crack length at which it happens for all probes is about 5 μm, approximately twice the film thickness. For all films tested, the crack length just before the crack-length jump was about twice the film thickness, regardless of what probe geometry was used.

B. Instrumented indentation

While traditional indentation fracture analyses rely on knowledge of the peak indentation load only, there is potentially much more information to be gleaned from the instrumented indentation response. Other work has correlated discontinuities in Berkovich load-displacement (P-h) behavior to fracture properties.[20–22] In this section, some phenomena that relate different types of cracking to features in the load-displacement traces, as well as the apparent indentation modulus, will be shown. The reason for this lengthy investigation is

that only radial fracture will be used to study the fracture properties of the films; competing fracture systems (such as lateral cracking[23]) can make the subsequent analysis much more complicated. The most illustrative examples have been chosen from amongst the different films, but the observations are broadly applicable.

Figure 3 is a P-h plot for the loading half-cycle for five 15-mN peak load Berkovich indentations on 2.4-μm LKB. The traces are segmented into three portions (shown on the figure) based on indentation load. Segment 1 is from zero load to a point where P-h discontinuity events (pop-in) begin. Toivola et al.[22] suggested that these events corresponded to fracture in low-κ films during Berkovich indentation. Segment 2 is the load range over which the pop-in event occur, 3.3–4.8 mN, and Segment 3 is at higher loads, where the P-h traces reconverge. The load range for pop-in was 2.2–2.9 mN for 1.6-μm-thick LKB and 1.8–2.4 mN for 0.8-μm-thick LKB, indicating that there probably is some influence of the substrate for Berkovich pop-in in low-κ films. Because no concerted effort was made to study the
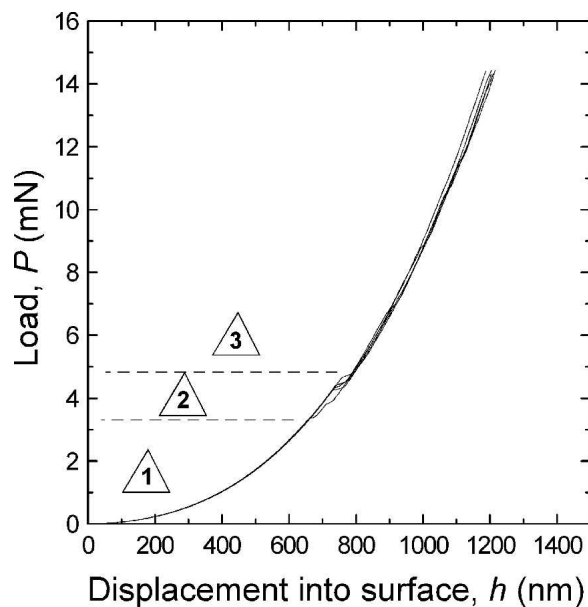
FIG. 3. *P-h* traces during the loading half-cycle for five 15-mN peak load Berkovich indentations on 2.4-μm-thick LKB. The traces are segmented into three regions of indentation load: (1) superposable traces at the smallest loads, (2) displacement excursions (pop-in) events, and (3) end of pop-in events and recovery of superposibility.

Berkovich pop-in phenomena (not all material-film thickness combinations were tested with the Berkovich), this is not explored further in this work.

Figure 4(a) is a plot of the apparent indentation modulus, $\bar{E}^{A}$, as a function of contact depth h_{c} from the same experiments in Fig. 3. This is the conventional manner of plotting indentation modulus. Also shown in Fig. 4(a) are the three segments from Fig. 3, transformed to segments of contact depth. $\bar{E}^{A}$ decreases sharply at the smallest contact depths, goes through an apparent minimum near 50 nm, and then begins to increase again with further increase in indenter penetration. The minimum at small contact depths is often observed for low-κ films.[24–26] The apparent modulus minimum has been attributed to difficulty in locating the point of first surface contact, or uncertainty in the contact area, although at this point this is simply conjecture. $\bar{E}^{A}$ then increases with increasing contact depth due to the increasing influence of the stiff substrate on the overall elastic response. There is a discontinuity in the elastic response that corresponds with the range of pop-in events. After the pop-in events cease, $\bar{E}^{A}$ again increases monotonically. Figure 4(b) is a plot of indentation modulus with respect to load, with the three load segments from Fig. 3 marked. Pop-in events, or at least the initial pop-in events during loading, do not affect the $\bar{E}^{A}$ response with respect to load. This is an important observation, and is contrasted with cube-corner indentation in the next paragraph. These observations agree with the previous observation of Morris et al.[6] that the quantity load-over-stiffness-squared (P/S^{2})[27] was
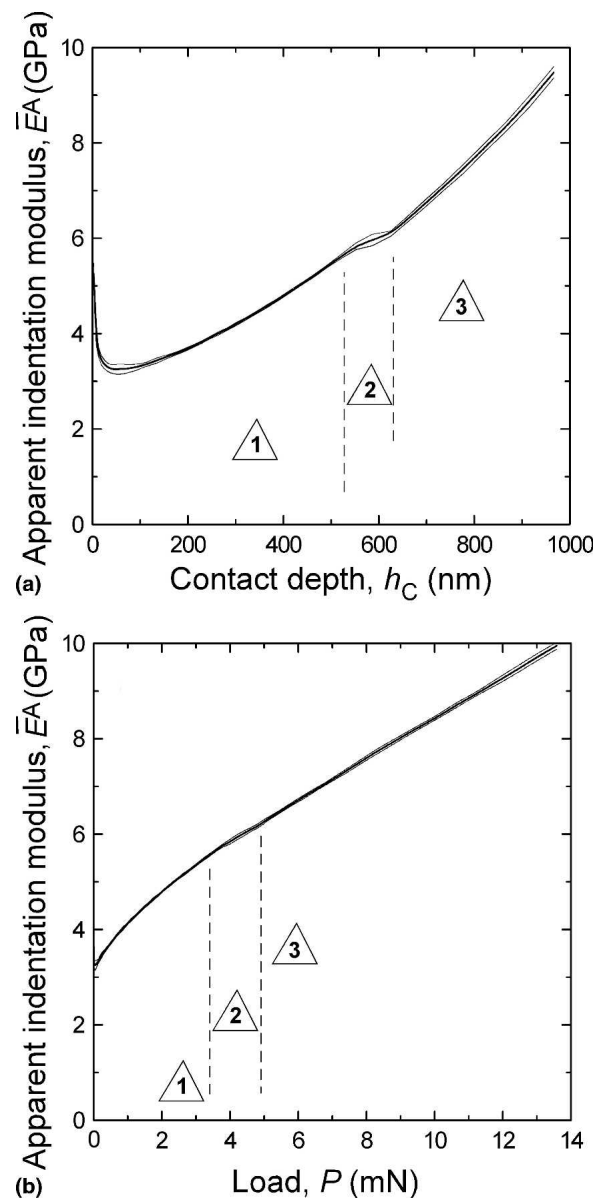

FIG. 4. (a) $\bar{E}^{A}$ as a function of h_{c} for Berkovich indentation on 2.4-μm-thick LKB. The bold line is the mean, and bracketing thin lines represent one standard deviation. Three segments in contact depth are marked, corresponding to the segments marked in Fig. 3. (b) $\bar{E}^{A}$ as a function of P with regions marked corresponding to the segments in Fig. 3.

unaffected by loading discontinuities that were attributable to radial fracture.

The Berkovich results, which suggest that the indentation modulus plotted with respect to load is unaffected by pop-in events, should now be compared to similar experiments with a cube-corner probe. Figure 5(a) is a *P-h* plot for five 22-mN peak load cube-corner indentations on 2.0-μm LKA. The entire indentation response has been divided into four segments of load, based on four different regions of behavior. Segment 1 is a region of no (or barely discernable) pop-in events, where the
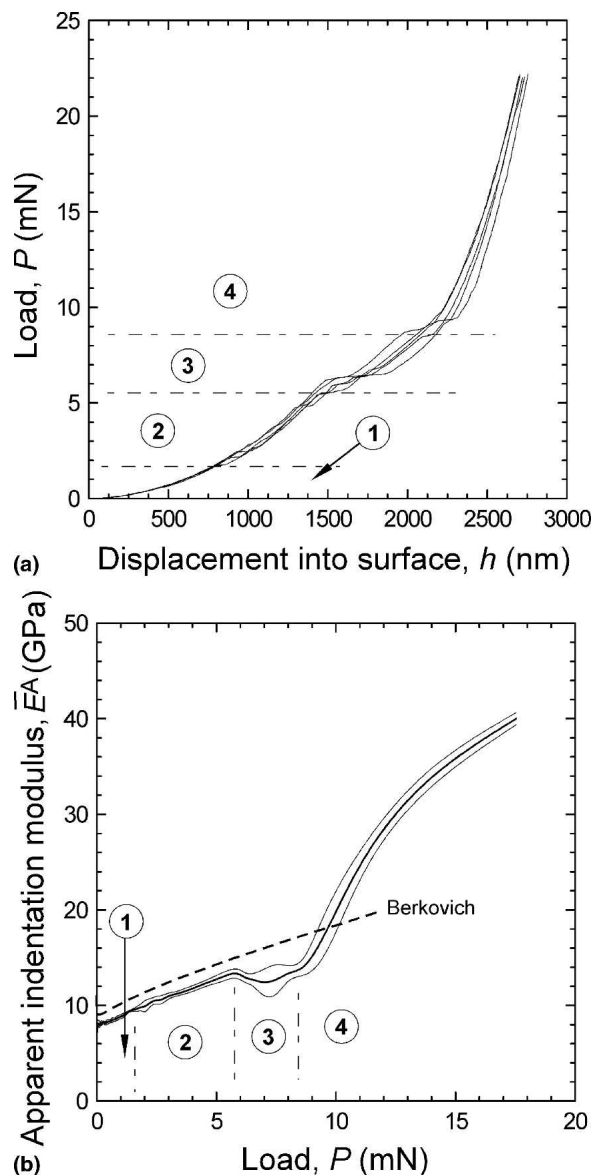
FIG. 5. (a) *P-h* traces during the loading half-cycle for five cube-corner indentations on 2-μm-thick LKA. The traces are segmented into four regions based on indentation load: (1) no apparent pop-in events, (2) small pop-in events, (3) larger pop-in events, (4) increasing stiffening of the contact. (b) Apparent indentation modulus as a function of indentation load. The apparent modulus from Berkovich indentation is shown as a dashed line for comparison.

P-h traces are essentially superposable. Segment 2 is a region of "small" pop-in events and segment 3 is a region of "large" pop-in events. In segment 4, the *P-h* responses smooth and stiffen, and appear to converge again to a unified response.

Figure 5(b) compares $\bar{E}^A$ for the 22-mN indentations shown in Fig. 5(a) as a function of load. Also shown for comparison is $\bar{E}^A$ as a function of P for the same material-thickness combination, measured with a calibrated Berkovich on the DCM instrument. Much like the Berkovich pop-in events of Fig. 3, the "small" pop-in regime

(segment 2) has little effect on the evolution of $\bar{E}^A$ versus P if perhaps there is a small increase in the experimental uncertainty (one standard deviation in measured $\bar{E}^A$, shown as thin lines bracketing the mean) in segment 2. However, in segment 3, the so-called "large" pop-in regime, the apparent modulus decreases, and the uncertainty in $\bar{E}^A$ increases greatly. After "large" pop-in deformation is exhausted, the $\bar{E}^A$-P relationship changes discontinuously, in contrast with the behavior of Berkovich indentation.

To explore this phenomena further, Fig. 6(a) is a *P-h* plot for two separate 1.5-mN cube-corner indentation experiments (peak loads within segment 2, Fig. 5) on 2.0-μm LKA. One trace exhibits pop-in events; another does not. Figure 6(b) is a SEM micrograph of the impression + fracture pattern generated by the indentation that does not exhibit pop-in; and Fig. 6(c) is a SEM micrograph of the impression + fracture pattern generated by the indentation that does exhibit pop-in. The only difference in the fracture at the indentation sites is the apparent ejection of a small amount of material at the lower right directly adjacent to the indentation.

Figure 7 is a series of representative SEM micrographs of cube-corner indentations to increasing peak loads on 2.0-μm-thick LKA; in the lower-left corner of each micrograph is a number that corresponds with the indentation load segments delineated in Fig. 5(a). Figure 7(a) is a sub-threshold 0.068-mN indentation. Only radial fracture is seen within segment 1 (no pop-in) for the 0.68-mN indentation in Fig. 7(b). The 4.6-mN indentation in Fig. 7(c), corresponding to segment 2 (small pop-in) in Fig. 5(a), shows radial fracture as well as a small lateral crack directly adjacent to the indentation impression. In Fig. 7(d), two of the surface traces of the radial cracks (the bottom and upper right cracks) in the 6.8-mN indentation shown have begun to curve near the tips. This is within the "large" pop-in segment (segment 3). For the 15-mN indentation in Fig. 7(e), the radial cracks have apparently bifurcated, and the tips continue to curve toward an approximately circumferential trajectory. Finally, the 50-mN indentation of Fig. 7(f), also within segment 4, shows that a large chip, or lateral crack, has formed and been ejected from the indentation site. The bottom of the large lateral crack is apparently smooth and flat. Presumably, this is the surface of the silicon, but no further experiments were done to confirm this.

Figure 8 is an isometric-view schematic diagram demonstrating the difference between the two types of lateral cracking systems. The "shallow lateral" cracks[23] have dimensions that are roughly the size of the impression side and have depths that are well contained within the film. The delamination or "deep lateral" cracks[23] form at higher indentation loads. Deep laterals or delaminations seem to initiate from the radial cracks that are generated at much smaller loads and have surface dimensions much
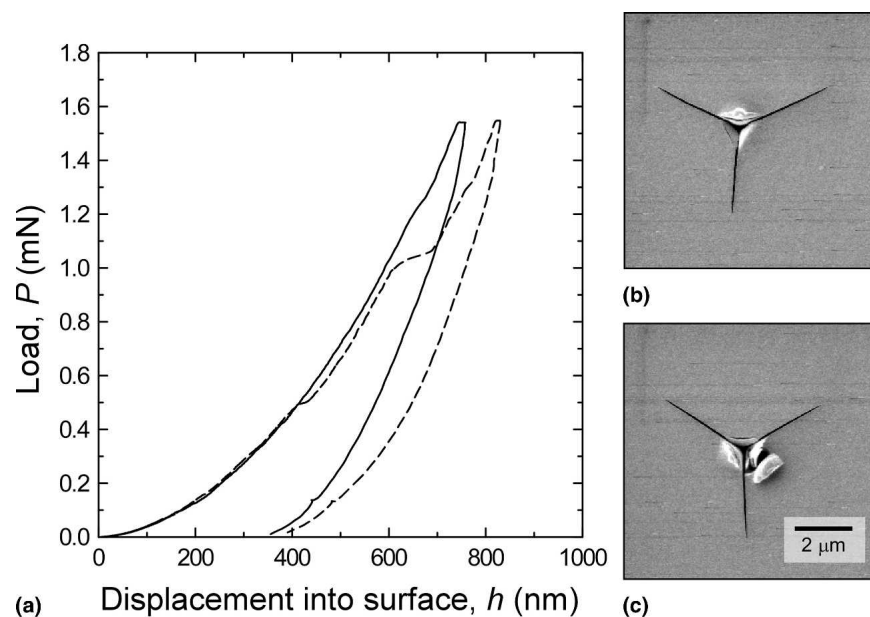
FIG. 6. (a) *P-h* traces for 1.55-mN peak load cube-corner indentations on 2-μm-thick LKA. One indentation (solid line) does not show pop-in; another (dashed line) shows two pop-in events. (b) SEM image corresponding to solid *P-h* trace. (c) SEM image corresponding to dashed *P-h* trace.

larger than the indentation impression or the film thickness. The micrograph of Fig. 7(f) suggests that the deep lateral crack front propagates laterally at, or close to, the silicon-film interface.

IV. DISCUSSION

A. Relationship between fracture and apparent elastic modulus responses

Section III showed that there is a definite connection between displacement discontinuities in the *P-h* response and the perceived elastic modulus. Small pop-in events shift the $\bar{E}^A$-h_c response, but leave the $\bar{E}^A$-P trace unaffected. Furthermore, the connection was made between the type of pop-in event (either "small" or "large") and the fracture event. Small pop-in corresponds with formation and ejection of very small lateral cracks, while large pop-in corresponds with the initiation and propagation of a large delamination crack.

Figures 9(a)–9(d) are a combined plot of *c* (left axis) and $\bar{E}^A$ (right axis) versus *P* for cube-corner indentation on 2.0-, 1.5-, 1.0-, and 0.5-μm-thick LKA, respectively. In each plot, the steep increase in $\bar{E}^A$ is correlated with the jump in crack length. What happens at the jump in radial crack length? The large pop-in events (Fig. 5) are indicative of the large lateral-delamination crack initiating and propagating subsurface. As the support of the film is lost, the probe makes contact with the stiff silicon substrate and the apparent elastic modulus increases dramatically. On the surface, an observer sees a jump in the radial crack length as the constraint of the substrate is lost, and now the radial-delamination crack system

propagates away from the indentation. The surface beginnings of the delamination scallop can be seen in Fig. 7(d), where the radial cracks have evidently started to curl into a circumferential trajectory. Increasing indentation load pries the delamination scallop off the surface and completes the removal of material, as seen in Fig. 7(f).

Figures 10(a)–10(c) are *c-P-$\bar{E}^A$* plots for 2.4-, 1.6-, and 1.2-μm-thick LKB, respectively. Figure 10(a) shows that the same correspondence between the steep increase in $\bar{E}^A$ and a jump in crack length. However, in Figs. 10(b) and 10(c), there is no evident jump in crack length, although it might be argued that the experimental scatter increases, or the *c-P* response becomes less "smooth." The lack of a jump in the crack length might indicate that the indenter has struck the silicon, without causing delamination.

B. Composite elastic modulus response

The *c-P-$\bar{E}^A$* plots are useful for pointing out what fracture data are radial, and which data are radial + delamination. It is also interesting to note that there appears to be a roughly load-independent plateau in $\bar{E}^A$ up to at least 0.5 mN for the three thickest LKA films, but the 0.5-μm LKA film already has a strong substrate influence above 0.1 mN. Compare this with Fig. 2(a), where crack lengths in all LKA films are roughly equal to a peak load of 0.5 mN, with the 0.5-μm LKA film being a notable exception. This suggests that perhaps there is a relationship between the fracture response and the apparent indentation modulus response.

There have been many proposed models that describe the composite elastic response of a film + substrate system
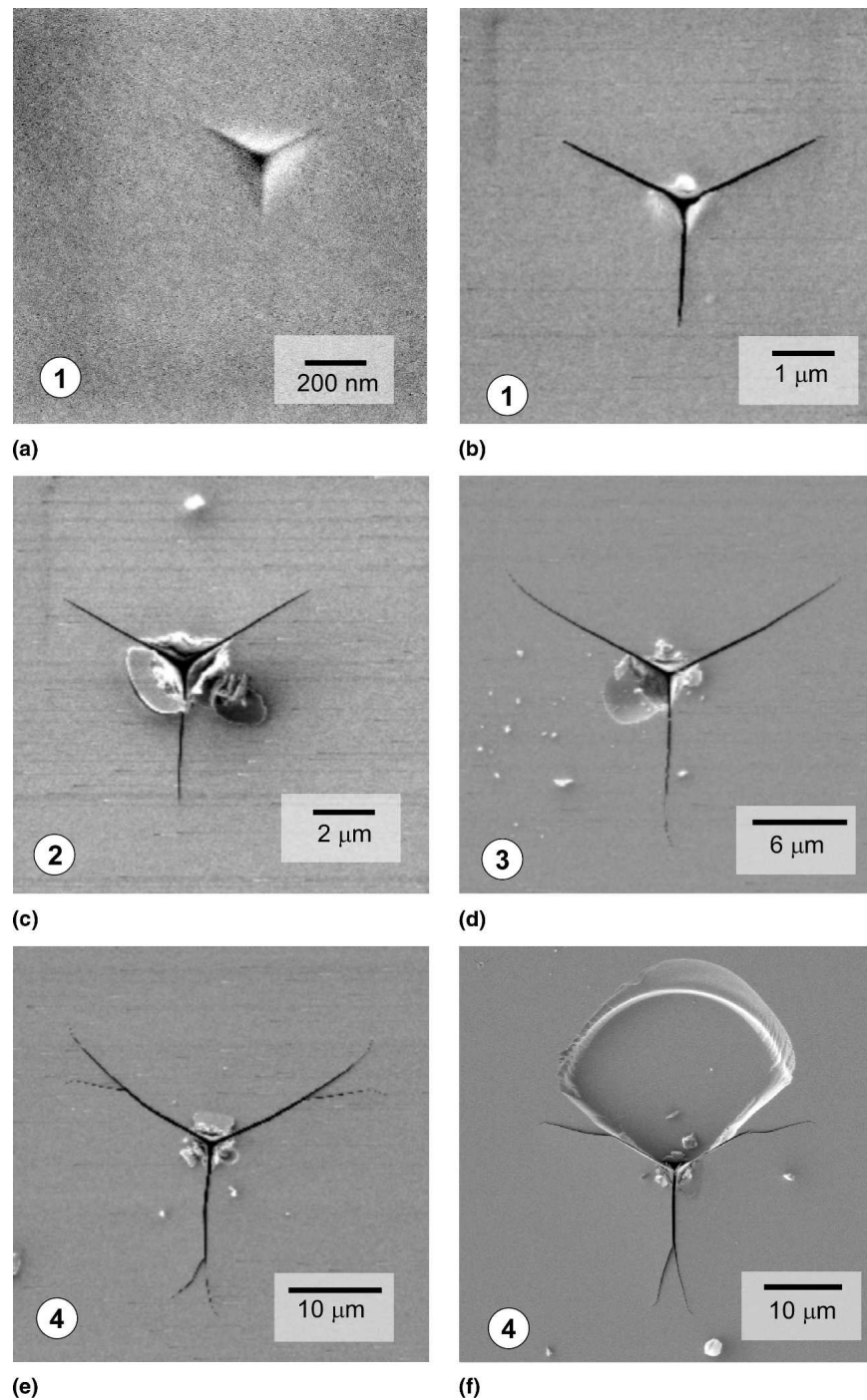
FIG. 7. Sequence of SEM images of cube-corner indentations on 2-μm-thick LKA to different peak loads. The indentation load region from Fig. 5 is shown in the lower left corner of each image. (a) 0.068-mN subthreshold indentation. (b) 0.68-mN peak load indentation; there are only radial cracks. (c) 4.6-mN peak load indentation; radial cracks and some small lateral cracking damage can be seen at the indentation site. (d) 6.8-mN peak load indentation; the radial cracks are much longer, and two of them are curved near the end. (e) 15-mN peak load indentation; the surface traces of the cracks have all turned and bifurcated. (f) 50-mN peak load indentation; a large lateral crack, or possibly a delamination event, has been ejected from the surface.

subjected to indentation.[28–34] Every one of these models suggests that $\bar{E}^A$ is some function of $\bar{E}^F$ and $\bar{E}^S$, as well as the ratio of the (axisymmetric equivalent) contact radius to film thickness a/t^F. Figure 11(a) is a plot of $\bar{E}^A$ versus a/t^F for 15-mN peak load indentation by each of four probes on 1.0-μm-thick LKA, and Fig. 11(b) is a similar plot of $\bar{E}^A$ versus a/t^F for 2.4-μm-thick LKB. In each case, the scaling of $\bar{E}^A$ with respect to a/t^F is the
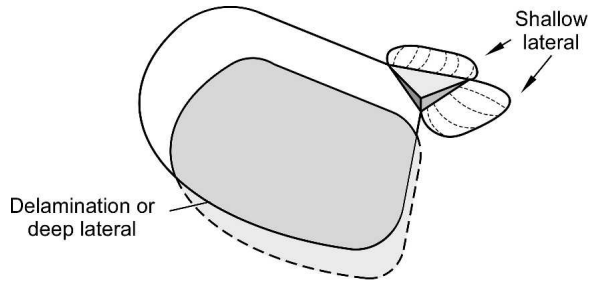
FIG. 8. Isometric schematic diagram showing the difference between the two types of lateral cracking that lead to pop-in events during sharp indentation on low-κ films.

same (for the 50° and cube-corner probes) until there is a sharp increase in $\bar{E}^A$ due to delamination and spalling at the indentation site.

One of the more explicitly physically based models is the perturbation analysis of Gao et al.[30] They derived an expression for $\bar{E}^A$ in terms of film and substrate shear modulus (μ) and Poisson's ratio (ν),

$$\frac{1}{\bar{E}^A} = \frac{1}{2} \frac{1 - (1 - I_1)\nu^S - I_1\nu^F}{(I - I_0)\,\mu^S + I_0\mu^F} \quad , \qquad (1)$$

where I_0 is the proportion of the total strain energy contained within the film, and I_1 is the proportion of dilatational strain energy contained within the film. It is clear from Eq. (1) that the composite plain-strain elastic compliance is formed by weighting the shear modulus and Poisson's ratio by the total and dilatational strain-energy distributions, respectively. Xu and Pharr modified the Gao analysis to arrive at the following expression for $\bar{E}^A$[34]:

$$\frac{1}{\bar{E}^A} = \frac{1}{2} \left[1 - (1 - I_1)\nu^S - I_1\nu^F \right] \left[(1 - I_0)\,\frac{1}{\mu^S} + I_0\,\frac{1}{\mu^F} \right] \quad . \qquad (2)$$

The Xu–Pharr representation, then, differs from the Gao representation by weighting the individual shear compliances by I_0. With the substitution $\eta = t^F/a$, I_0 and I_1 are[30]

$$I_0 = \frac{2}{\pi} \arctan \eta + \frac{1}{2\pi(1 - \nu)} \left[(1 - 2\nu)\eta \, \ln\left(\frac{1 + \eta^2}{\eta^2}\right) \right.$$
$$\left. - \frac{\eta}{1 + \eta^2} \right] \quad , \qquad (3)$$

$$I_1 = \frac{2}{\pi} \arctan \eta + \frac{\eta}{\pi} \ln\left(\frac{1 + \eta^2}{\eta^2}\right) \quad . \qquad (4)$$
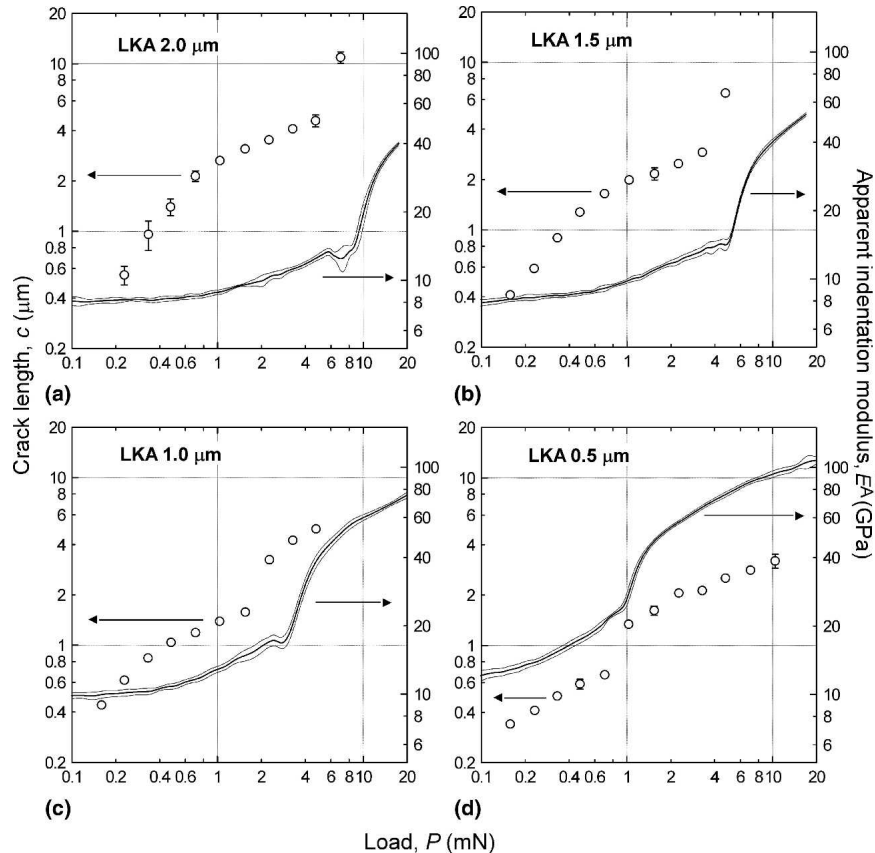

(a)

(b)

(c)

(d)

Load, P (mN)

FIG. 9. c and $\bar{E}^A$ as a function of P for cube-corner indentation on LKA films. The bold line is the mean apparent indentation modulus and the thin bracketing lines represent one standard deviation.

(a)

(b)

(c)

Load, P (mN)

FIG. 10. c and $\bar{E}^{A}$ as a function of P for cube-corner indentation on LKB films. The bold line is the mean apparent indentation modulus and the thin bracketing lines represent one standard deviation.
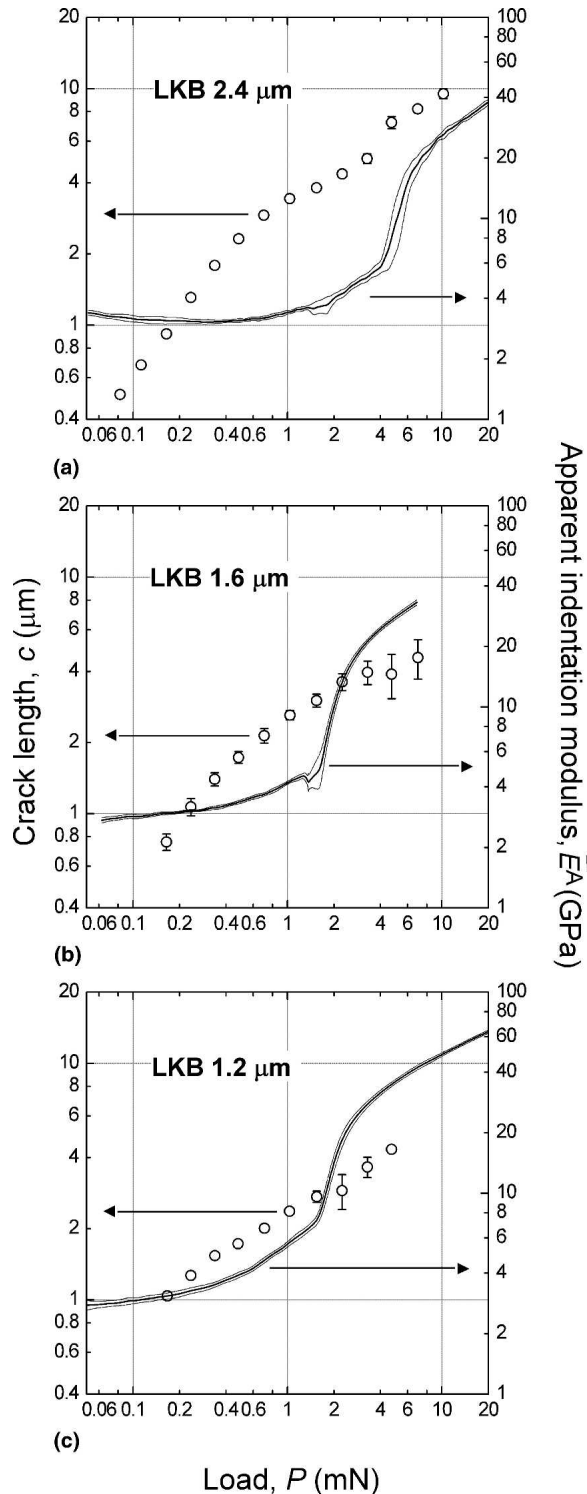
There is a ν associated neither with the film nor the substrate in the expression for I_0 [Eq. (3)]. This is a higher-order term, a consequence of the first-order perturbation analysis.[30] Figure 12 plots I_0 and I_1 versus a/t^{F}
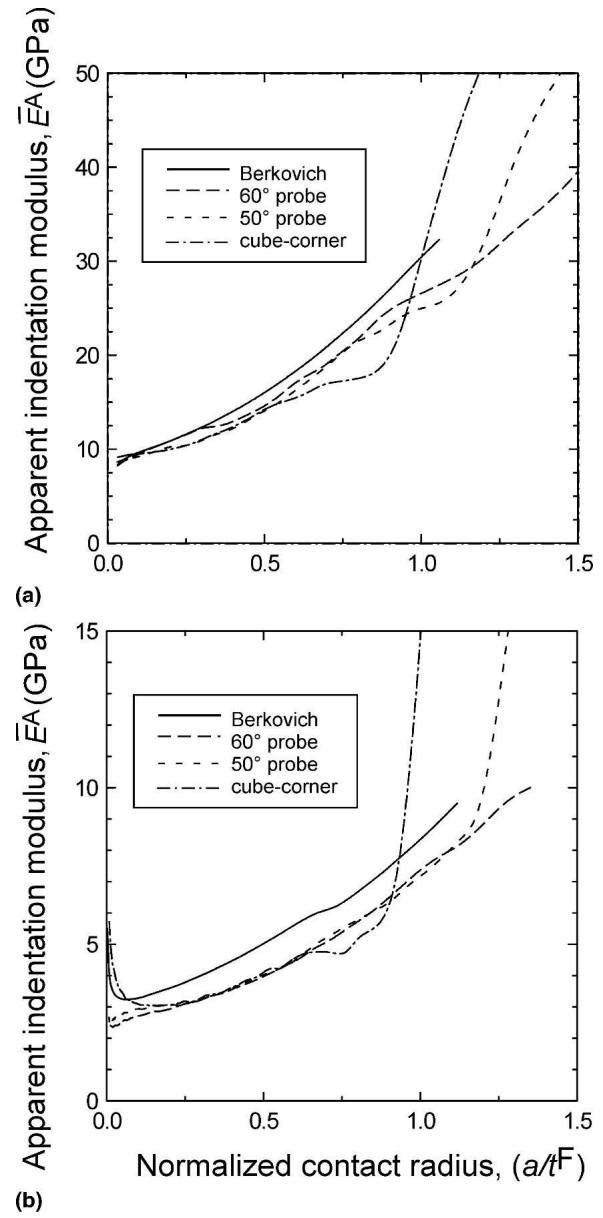

(a)

(b)

FIG. 11. $\bar{E}^{A}$ as a function of normalized contact radius, a/t^{F}, from four pyramidal probes of varying acuity for (a) 1.0-µm LKA and (b) 2.4-µm LKB.

over the range $0 \leqslant a/t^{F} \leqslant 2$. It can be seen that I_1 decreases more slowly than I_0 with increasing a/t^{F}, no matter what Poisson's ratio is used in Eq. (3). This suggests that when the composite indentation modulus is formed at large a/t^{F}, the effects of Poisson's ratio mismatch will be less important than shear moduli mismatch.

A few simplifications of Eq. (2) can be made to make the influence of strain-energy partitioning on $\bar{E}^{A}$ more apparent. If, in fact, contributions to the composite indentation modulus from Poisson's ratio are less important than those from the shear moduli, Eq. (2) may be rewritten as
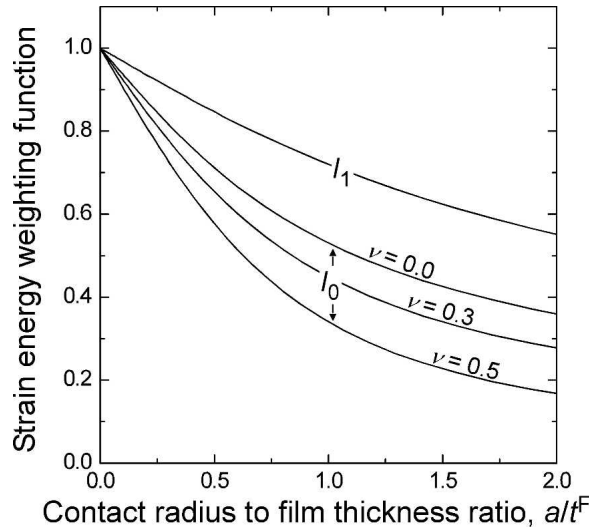
FIG. 12. Total (I_0) and dilatational (I_1) strain energy weighting functions of Eqs. (3) and (4).

$$\bar{E}^A \cong \frac{\bar{E}^S \bar{E}^F}{\bar{E}^F + I_0 (\bar{E}^S - \bar{E}^F)} \quad . \tag{5}$$

Approximation of Eq. (5) with $\bar{E}^S \gg \bar{E}^F$ and the binomial expansion leads to a simple scaling relationship for the apparent modulus of a film on a rigid substrate:

$$\bar{E}^A \cong \frac{\bar{E}^F}{I_0} \quad , \tag{6}$$

which indicates that the apparent increase in modulus is inversely proportional to the fraction of strain energy in the film. The Gao representation, in the limit $\bar{E}^S \gg \bar{E}^F$, is approximately

$$\bar{E}^A \cong (1 - I_0) \, \bar{E}^S \quad . \tag{7}$$

The limiting cases of Eqs. (6) and (7) show simply why the Xu–Pharr representation has been shown to be a significant improvement on the Gao representation for compliant films,[31] even though both models converge to the film or substrate response as $a/t^F \rightarrow 0$ or $a/t^F \rightarrow \infty$, respectively. As has been pointed out,[34] Eq. (2) is most closely connected to the film elastic properties, while the Gao representation is chiefly tied to the substrate modulus for very compliant films.

Figure 11 demonstrates that the composite elastic response for probes of differing acuity could be reduced to a single function of a/t^F, in accordance with nearly all layered-media contact models. Under the pressures of indentation, a compliant film is locally reduced to a thickness substantially less than the original thickness t^F. It has been observed that the agreement between theory and experiment for both the Gao model[32] and Song–Pharr model[31] (closely related to the Xu–Pharr model) is greatly increased when an effective thickness, t^F_{eff} is sub-

stituted for t^F in Eq. (1) to compensate for film deformation. Rar et al.[31] showed that the use of $t^F_{eff} = t^F - h_c$ worked well for Berkovich indentation.

Equations (5)–(7) are all easily implemented for data-fitting purposes, but the simplified Xu–Pharr expressions, Eqs. (5) and (6), will be most useful for representation of low-κ film moduli from composite indentation data. The Song correction for film thickness reduction, $t^F_{eff} = t^F - h_c$ is used to correct the film thickness to follow the scaling form of Eq. (6). Figure 13 is a plot of $\bar{E}^A$ (from Berkovich indentation experiments) as a function of a/t^F_{eff} for the thickest of each variety of low-κ film. Also shown in Fig. 13 are ordinary least-squares fits of Eq. (6), $\bar{E}^A = \bar{E}^F/I_0$ to each film $\bar{E}^A$ response. The rigid-substrate limit of the Song model has a remarkable ability to reproduce the apparent modulus response of low-κ films with increasing indenter penetration, considering that $\bar{E}^A$ is the only adjustable parameter. The value of $\bar{E}^F$ from the fit is the value reported in Table I.

Of course, the effective film correction appropriate to the Berkovich would not work for the non-Berkovich indenters, as the contact depth is greater for equivalent contact radius, but Fig. 11 demonstrates that under the simple a/t^F transformation the curves from various probes are approximately coincident if delamination is avoided. The real utility of this model as concerns the current work is not its extrapolative accuracy, but for its physical interpretation. That is, the strain-energy partition between film and substrate may be estimated experimentally as $I_0 = \bar{E}^F/\bar{E}^A$.
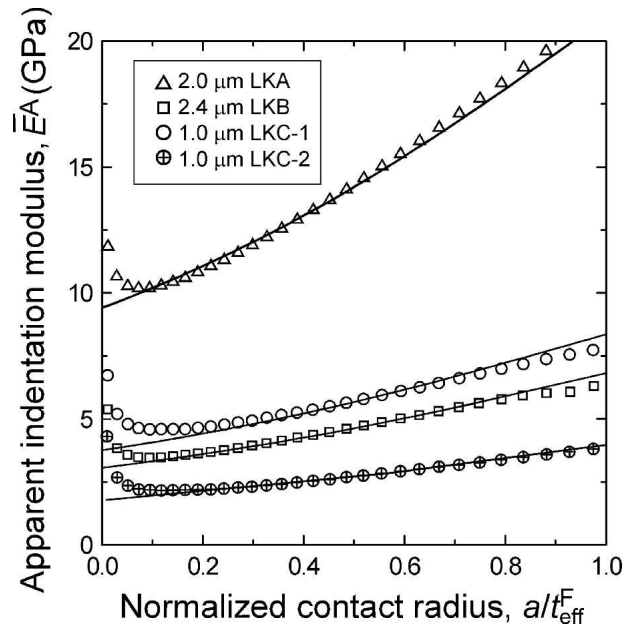

FIG. 13. $\bar{E}^A$ from Berkovich indentation as a function of corrected normalized contact radius, $a/(t^F - h_c)$ for the thickest of each variety of low-κ film. Shown for each film is a best-fit $\bar{E}^A$ response from the rigid-substrate limit of Eq. (6).

Let us revisit the introduction to this section, which noted a correspondence between the apparent modulus and the fracture response. Again, take as an example the LKA *c-P* data in Fig. 2(a). All film thicknesses, except the 0.5-μm-thick film, have the same fracture and elastic responses up to an indentation load of about 0.46 mN. After this point, the *c-P* responses of the thinner films start to peel away in order of increasing thickness. This is also the order in which the indenting probe starts to "feel" the elastic influence of the stiff substrate in the film.

By the argument made above, the fraction of total indentation work supplied to the film can be estimated by $I_0 = \bar{E}^F/\bar{E}^A$. Clearly, the increase in apparent modulus with increasing load is a signal that elastic indentation energy is being lost to the substrate. The relative loss of strain energy to the substrate is remarkably rapid. For example, consider the LKB material with $\bar{E}^F$, adhered to a silicon substrate of $\bar{E}^S = 170$. Limiting values of $\bar{E}^A$ are therefore $\bar{E}^F$ at small indentation loads and $\bar{E}^S$ at large loads. As indentation load is increased, $\bar{E}^A$ would increase quickly from $\bar{E}^F$. When the apparent modulus is double that of $\bar{E}^F$, half of the indentation strain energy is in the substrate; yet, $\bar{E}^A$ is only 3.6% of the limiting value (of 170 GPa).

Continuing with the same example of cube-corner indentation of LKA at an indentation load of 0.46 mN, the fraction of total indentation energy within the film is $\simeq$50% (0.5 μm thick), $\simeq$80% (1.0 μm thick), and $\simeq$100% (1.5- and 2.0-μm-thick LKA). The crack lengths in each film, as a percentage of those in 2.0 μm thick LKA, are 42% (0.5 μm thick), 74% (1.0 μm thick), 89%, and 100% (for 1.5 μm thick and 2.0 μm thick). The fraction of energy lost to the substrate and the reduction in crack length track neatly. In short, loss of strain energy to the substrate seems to explain why at fixed indentation load, thinner films tend to have shorter crack lengths. The connection between strain-energy partitioning and the fracture response will be explored in more detail for the fracture mechanics model in Part II.[5]

V. SUMMARY

It has been demonstrated that indentation flaws can be reliably and repeatably placed in low-κ films with the use of an ultra-low load, depth-sensing indenter, and a probe of sufficient acuity. Here, the main observations of indentation on low-κ films are summarized, with a focus on indentation fracture.

Berkovich indenters are insufficiently acute to generate real radial fracture outside the contact zone, although images of the indentations may appear to have radial cracks. More acute pyramidal probes, however, can generate stable radial fracture. Comparison of crack length to the contact dimension derived from instrumented inden-

tation can distinguish radial fracture from cutting or crushing.

The crack length versus load results on different compositions of organosilicate low-κ film, of varying thickness, show no clear scaling trends. Furthermore, there is a variation with film thickness that is not accounted for in current indentation fracture models.

The apparent elastic modulus versus load response is unaffected by small pop-in events, regardless of indenter acuity.

A discontinuity in the crack length versus load plot coincides with a discontinuity in the apparent indentation modulus for cube-corner indenters.

The discontinuities in crack length and apparent indentation modulus are due to film delamination, which is not immediately evident from SEM images.

The apparent indentation modulus for these film–substrate systems scales as the normalized contact radius, independently of the indenter acuity, in accordance with most contact models.

The Xu–Pharr model, which relates the apparent indentation modulus to proportion of strain energy contained in the film and substrate, can describe the apparent indentation modulus of low-κ films as a function of normalized contact radius.

An increase in apparent modulus indicates that an increasing proportion of indentation strain energy is being sunk into the substrate. Strain energy lost to the substrate leads to shortened crack lengths.

The Berkovich geometry is far and away the most studied indenter geometry in the instrumented indentation literature, and consequently accurate measurement of hardness and plane-strain modulus with the Berkovich is a well-developed art. However the Berkovich evidently cannot generate radial fracture in low-κ films. Of course, simultaneous measurement of hardness and modulus with more acute geometries while performing fracture experiments would be advantageous by saving time. At this point, we could not recommend using the acute, radial-fracture generating geometries to accurately measure hardness and moduli when a Berkovich indenter is available. This recommendation is partially because of the difficulty of area-function calibration when there is cracking at the indentation, and partially because of the inferior development of hardness and modulus measurement for non-Berkovich sharp indenters. Continuous estimation of indentation modulus with the acute indenters, while perhaps not as accurate as possible, compares well with Berkovich indenters and can also reveal information about the nature of the fracture at the indentation site.

To the best of the authors' knowledge, the current development of experimental technique and observations have not been made previously in the indentation fracture literature and are essential to the fracture mechanics model developed in the companion paper, Part II.[5] It is

hoped that the observations made here are useful to experimentalists working with fracture, or other problems, concerning indentation on film-substrate systems. More observations of indentation on these particular films, especially with indenters other than the cube-corner, are available elsewhere.[35]

ACKNOWLEDGMENT

Certain commercial equipment, instruments, or materials are identified in this paper to foster understanding. Such identification does not imply recommendation or endorsement by the National Institute of Standards and Technology, nor does it imply that the materials or equipment identified are necessarily the best available for the purpose.

REFERENCES

1. International Technology Roadmap for Semiconductors, 2006 Update, Assembly and Packaging. http://www.itrs.net (accessed 2006), p. 2.
2. G.R. Anstis, P. Chantikul, B.R. Lawn, and D.B. Marshall: A critical evaluation of indentation techniques for measuring fracture toughness. I. Direct crack measurements. *J. Am. Ceram. Soc.* **64,** 533 (1981).
3. B.R. Lawn: *Fracture of Brittle Solids* (Cambridge University Press, Cambridge, UK, 1993).
4. A. Arora, D.B. Marshall, B.R. Lawn, and M.V. Swain: Indentation deformation/fracture of normal and anomalous glasses. *J. Non-Cryst. Solids* **31,** 415 (1979).
5. D.J. Morris and R.F. Cook: Indentation fracture of low-dielectric constant films: Part II. Indentation fracture mechanics model. *J. Mater. Res.* **23,** 2443 (2008).
6. D.J. Morris, S.B. Myers, and R.F. Cook: Sharp probes of varying acuity: Instrumented indentation and fracture behavior. *J. Mater. Res.* **19,** 165 (2004).
7. B.N. Lucas, W.C. Oliver, G.M. Pharr, and J.L. Loubet: Time dependent deformation during indentation testing, in *Thin Films: Stresses and Mechanical Properties VI*, edited by W.W. Gerberich, H. Gao, J-E. Sundgren, and S.P. Baker (Mater. Res. Soc. Symp. Proc. **436,** Pittsburgh, PA, 1997), p. 233.
8. W.C. Oliver and G.M. Pharr: An improved technique for determining hardness and elastic modulus using load and displacement sensing indentation experiments. *J. Mater. Res.* **7,** 1564 (1992).
9. B.N. Lucas, W.C. Oliver, and J.E. Swindeman: The dynamics of frequency-specific, depth-sensing indentation testing, in *Fundamentals of Nanoindentation and Nanotribology*, edited by N.R. Moody, W.W. Gerberich, N. Burnham, and S.P. Baker (Mater. Res. Soc. Symp. Proc. **522,** Warrendale, PA, 1998), p. 3.
10. W.C. Oliver and G.M. Pharr: Measurement of hardness and elastic modulus by instrumented indentation: Advances in understanding and refinements to methodology. *J. Mater. Res.* **19,** 3 (2004).
11. K. Ikezawa and T. Maruyama: Sharp tip geometry and its effect on hardness in nanoindentation experiments. *J. Appl. Phys.* **91,** 9689 (2002).
12. G.M. Pharr, D.S. Harding, and W.C. Oliver: Measurement of fracture toughness in thin films and small volumes using nanoindentation methods, in *Mechanical Properties and Deformation Behavior of Materials Having Ultra-Fine Microstructures*, edited by M. Nastasi, D.M. Parkin, H. Gleiter (NATO ASI, Boston, MA, 1993), p. 449.
13. K. Kese and D.J. Rowcliffe: Nanoindentation method for measuring residual stress in brittle materials. *J. Am. Ceram. Soc.* **86,** 811 (2003).
14. D.J. Morris and R.F. Cook: In situ cube-corner indentation of soda-lime glass and fused silica. *J. Am. Ceram. Soc.* **87,** 1494 (2004).
15. S. Lathabai, J. Rodel, T. Dabbs, and B.R. Lawn: Fracture mechanics model for subthreshold indentation flaws. I. Equilibrium fracture. *J. Mater. Sci.* **26,** 2157 (1991).
16. R. Dal Maschio: Application of the Hagan model for crack nucleation to radial cracks in glass. *J. Mater. Sci. Lett.* **4,** 948 (1985).
17. B.R. Lawn and A.G. Evans: A model for crack initiation in elastic/plastic indentation fields. *J. Mater. Sci.* **12,** 2195 (1977).
18. R.F. Cook and L.M. Braun: Trapped cracks at indentations. II. Fracture mechanics model. *J. Mater. Sci.* **29,** 2192 (1994).
19. D.J. Morris and R.F. Cook: Radial fracture during indentation by acute probes: I, Description by an indentation wedging model. *Int. J. Fract.* **136,** 237 (2005).
20. S. Kim, Y. Toivola, R.F. Cook, K. Char, S-H. Chu, J-K. Lee, D.Y. Yoon, and H-W. Rhee: Organosilicate spin-on glasses. I. Effect of chemical modification on mechanical properties. *J. Electrochem. Soc.* **151,** 37 (2004).
21. Y. Toivola, K. Suhan, R.F. Cook, K. Char, J-K. Lee, D.Y. Yoon, H-W. Rhee, S.Y. Kim, and M.Y. Jin: Organosilicate spin-on glasses. II. Effect of physical modification on mechanical properties. *J. Electrochem. Soc.* **151,** 45 (2004).
22. Y. Toivola, J. Thurn, and R.F. Cook: Structural, electrical, and mechanical properties development during curing of low-*k* hydrogen silsesquioxane films. *J. Electrochem. Soc.* **149,** 9 (2002).
23. R.F. Cook and G.M. Pharr: Direct observation and analysis of indentation cracking in glasses and ceramics. *J. Am. Ceram. Soc.* **73,** 787 (1990).
24. A.A. Volinsky and W.W. Gerberich: Nanoindentaion techniques for assessing mechanical reliability at the nanoscale. *Microelectron. Eng.* **69,** 519 (2003).
25. X. Huang and A.A. Pelegri: Nanoindentation measurements on low-k porous silica thin films spin coated on silicon substrates. *J. Eng. Mater.-T. ASME* **125,** 361 (2003).
26. L. Shen and K. Zeng: Comparison of mechanical properties of porous and non-porous low-k dielectric films. *Microelectron. Eng.* **71,** 221 (2004).
27. D.L. Joslin and W.C. Oliver: A new method for analyzing data from continuous depth-sensing microindentation tests. *J. Mater. Res.* **5,** 123 (1990).
28. E.H. Yoffe: The elastic compliance of a surface film on a substrate. *Philos. Mag. Lett.* **77,** 69 (1998).
29. M.T. Kim: Influence of substrates on the elastic reaction of films for the microindentation tests. *Thin Solid Films* **283,** 12 (1996).
30. H. Gao, C-H. Chiu, and J. Lee: Elastic contact versus indentation modeling of multi-layered materials. *Int. J. Solids Struct.* **29,** 2471 (1992).
31. H. Song, G.M. Pharr, and A. Rar: Assessment of new relation for the elastic compliance of a film-substrate system, in *Thin Films: Stresses and Mechanical Properties IX*, edited by C.S. Ozkan, L.B. Freund, R.C. Cammarata, and H. Gao (Mater. Res. Soc. Symp. Proc. **695,** Warrendale, PA, 2002), p. 431.
32. J. Mencik, D. Munz, E. Quandt, E.R. Weppelmann, and M.V. Swain: Determination of elastic modulus of thin layers using nanoindentation. *J. Mater. Res.* **12,** 2475 (1997).
33. A. Perriot and E. Barthel: Elastic contact to a coated half-space: Effective elastic modulus and real penetration. *J. Mater. Res.* **19,** 600 (2004).
34. H. Xu and G.M. Pharr: An improved relation for the effective elastic compliance of a film/substrate system during indentation by a flat cylindrical punch. *Scr. Mater.* **55,** 315 (2006).
35. D.J. Morris: Indentation fracture of low-dielectric constant materials. Ph.D. Thesis, University of Minnesota, Minneapolis, MN (2004).